

# The effect of feedback on the emission properties of the Warm-Hot Intergalactic Medium

M. Roncarelli<sup>1</sup>, N. Cappelluti<sup>2,3</sup>, S. Borgani<sup>4,5,6</sup>, E. Branchini<sup>7,8,9</sup> and L. Moscardini<sup>1,2,10</sup>

<sup>1</sup>Università di Bologna, Dipartimento di Astronomia, via Ranzani 1, I-40127 Bologna, Italy

<sup>2</sup>INAF-Osservatorio Astronomico di Bologna, Via Ranzani 1, 40127 Bologna, Italy

<sup>3</sup>University of Maryland, Baltimore County, 1000 Hilltop Circle, Baltimore, MD 21250, USA

<sup>4</sup>Università di Trieste, Dipartimento di Fisica, Sezione di Astronomia, Via Tiepolo 11, I-34143 Trieste, Italy

<sup>5</sup>INAF-Osservatorio Astronomico di Trieste, Via Tiepolo 11, I-34143 Trieste, Italy

<sup>6</sup>INFN, Sezione di Trieste, Via Valerio 2, I-34127 Trieste, Italy

<sup>7</sup>Università degli Studi “Roma Tre”, Dipartimento di Fisica “E. Amaldi”, via della Vasca Navale 84, I-00146, Roma, Italy

<sup>8</sup>INFN, Sezione di “Roma Tre”, via della Vasca Navale 84, I-00146, Roma, Italy

<sup>9</sup>INAF, Osservatorio Astronomico di Brera, via Brera 28, I-20121, Milano, Italy

<sup>10</sup>INFN, Sezione di Bologna, viale Berti Pichat 6/2, I-40127 Bologna, Italy

17 April 2018

## ABSTRACT

At present, 30–40 per cent of the baryons in the local Universe is still undetected. According to theoretical predictions, this gas should reside in filaments filling the large-scale structure (LSS) in the form of a Warm-Hot Intergalactic Medium (WHIM), at temperatures of  $10^5 - 10^7$  K, thus emitting in the soft X-ray energies via free-free interaction and line emission from heavy elements. In this work we characterize the properties of the X-ray emission of the WHIM, and the LSS in general, focusing on the influence of different physical mechanisms, namely galactic winds (GWs), black-hole feedback and star-formation, and providing estimates of possible observational constraints. To this purpose we use a set of cosmological hydrodynamical simulations that include a self-consistent treatment of star-formation and chemical enrichment of the intergalactic medium, that allows us to follow the evolution of different metal species. We construct a set of simulated light-cones to make predictions of the emission in the 0.3–10 keV energy range. We obtain that GWs increase by a factor of 2 the emission of both galaxy clusters and WHIM. The amount of oxygen at average temperature and, consequently, the amount of expected bright OVII and OVIII lines is increased by a factor of 3 due to GWs and by 20 per cent when assuming a top-heavy IMF. We compare our results with current observational constraints and find that the emission from faint groups and WHIM should account from half to all of the unresolved X-ray background in the 1–2 keV band.

**Key words:** Cosmology: theory, large-scale structure of Universe – X-rays: diffuse background, galaxies: clusters – methods: hydrodynamical simulations

## 1 INTRODUCTION

The amount of baryonic matter present in the Universe is nowadays measured with high accuracy in the framework of the standard cosmological  $\Lambda$ -cold dark matter ( $\Lambda$ CDM) scenario. According to the most recent CMB observations (Komatsu et al. 2011) the percentage of baryonic density with respect to the critical one is  $100 \Omega_b = 4.49 \pm 0.28$ , a figure which is in excellent agreement with the estimates coming from the primordial nucleosynthesis of the heavy elements (Kirkman et al. 2003) and with the baryon budget at high redshift estimated from Ly $\alpha$  absorption systems (Weinberg et al. 1997; Rauch 1998), thus representing one of

the most important result of modern cosmology. Even if they constitute a minor component in the matter-energy budget, baryons are indeed crucial because, since they interact with the electromagnetic field, they are responsible for all the radiative phenomena, thus providing us the only probe to unveil also the dark components.

On the other side baryons associated to Ly $\alpha$  absorbers at the present epoch account for only  $\sim 30$  per cent of the cosmic mean (Penton et al. 2004; Bregman 2007). Indeed, when the cosmic structures form, the baryon census becomes much more challenging and it requires observations at different wavelengths. Despite the great improvements in our observational capabilities in the

last decade, when accounting for all the matter observed from the optical band (stars) to the X-rays (clusters) at  $z \lesssim 2$  the amount of observed gas in the Universe is much lower than expected. More precisely, about 30–40 per cent of the gas is still out of reach from current observational instruments (see Nicastro et al. 2005a, for a review): this issue is currently referred to as the “missing baryons” problem.

The first attempts to address this matter from the theoretical point view come from hydrodynamical simulations (Cen & Ostriker 1999; Davé et al. 2001) that showed that when galaxy clusters form, a significant amount of the whole intergalactic medium (IGM) remains out of the virialised halos creating a network of filaments, the so-called cosmic web (Bond et al. 1996), that provide a continuous flow of accreting material to the clusters themselves, located at the knots of the structure. The gas in these filaments remains at moderate overdensities ( $\delta \approx 10 - 10^3$ ) and is shock-heated up to temperatures of the order of  $10^5 - 10^7$  K, and is usually addressed as the Warm-Hot Intergalactic Medium (WHIM). Given its thermodynamical conditions the hydrogen and helium are fully ionized and emit via free-free interaction with the electrons. This process together with the line-emission from partly ionized metals is expected to contribute to the X-ray background (XRB) in the form of a soft diffuse component.

Analysing the current observational constraints, the unresolved emission in the *Chandra* Deep Fields (CDFs) observed by Hickox & Markevitch (2007) in the 0.5–1 keV band is consistent with the expectations of the diffuse gas obtained from numerical simulations (see, e.g., Roncarelli et al. 2006). Moreover, Galeazzi et al. (2009) detected the signature of a possible WHIM emission in the correlation function of the diffuse emission signal in the 0.4–0.6 keV band obtained from several *XMM-Newton* observations. On the other side, there have also been claims of detection of WHIM emission associated to local overdensities of the LSS. Werner et al. (2008) observed at  $5\sigma$  a continuum emission from a filament extending between the Abell 222 and Abell 225 clusters. Similarly, *ROSAT* observations allowed the discovery of a soft diffuse emission consistent with  $T \approx 10^6$  K gas associated with a galaxy group at  $z \sim 0.45$  (Zappacosta et al. 2002) and with the Sculptor supercluster (Zappacosta et al. 2005).

Probably the most important point in WHIM observation strategies is the fact that this medium is believed to contain metals whose emission and absorption lines provide an effective way to disentangle its signal from background and foreground objects. To this purpose, the best targets are C, O, Ne and possibly also N, Mg and Fe. The brightest features are expected from K and L-shell transitions of H-like, He-like and Li-like oxygen ions, namely the OVIII  $1s-2p$  doublet ( $E = 654$  eV), the OVII  $1s-2p$  resonance line (574 eV) and the OVI doublet (12 eV), respectively. This method already provided several claimed detections, all regarding absorption lines. Danforth & Shull (2005, 2008) detected 83 OVI absorption systems in the UV spectra of 43 AGNs. However, since these absorbers are associated to Ly $\alpha$  counterparts it is not clear how much of this gas can be attributed to the missing part (Tripp et al. 2008). At X-ray energies Nicastro et al. (2005b) detected several OVII absorption features in the spectra of the Mrk 421 blazar, but the statistical significance of their measurements has been questioned (Kaastra et al. 2006; Rasmussen et al. 2007; Yao et al. 2011). Several other detections with both *Chandra* (Fang et al. 2002; Mathur et al. 2003; Zappacosta et al. 2010) and *XMM-Newton* (Fujimoto et al. 2004; Takei et al. 2007; Buote et al. 2009; Fang et al. 2010) have been claimed but their statistical significance is low and they mainly correspond to the densest part of the IGM (galaxy clusters or groups),

indicating that these measurements are at the limit of current observational capabilities.

Up to now the detection of emission lines has proven to be even more difficult. However, detecting the WHIM in emission can be much more rewarding since it has the potential to map large structures and does not depend on the presence of background sources, thus potentially providing a global picture of WHIM thermo- and chemo-dynamics, which is by now far from being reached.

In this scenario a big effort has been put into the modelisation of the WHIM which becomes crucial in the perspective of future X-ray missions in particular for what concerns the treatment of radiative cooling, stellar and galactic feedback, reionization and, most importantly, chemical enrichment. Cen & Ostriker (2006) and Cen & Fang (2006) included for the first time the enrichment from Type II supernovae (SN-II) of different metal species in their Eulerian cosmological simulations. Their work showed how the effect of different galactic wind models can change both the thermodynamics and the abundance outside clusters. More recently Bertone et al. (2010) used a similar approach with a set of several large-scale simulations performed with the GADGET-3 code, including also Type Ia supernovae (SN-Ia) and asymptotic giant branch (AGB) stars to study specifically the properties of metal line emission.

In this work we use the set of cosmological hydrodynamical simulations of Tornatore et al. (2010) to study and characterize the emission of the WHIM, with particular emphasis on the of impact different enrichment schemes. Starting from the outputs of these simulations, we adopt a light-cone reconstruction approach in order to provide a more direct comparison with current and future observational constraints.

This paper is organized as follows. In the next section we will describe the simulation set of Tornatore et al. (2010) which constitutes the basis of our study. In Section 3 we will explain our method to create the mock light-cones and spectra from the outputs of the hydrodynamical simulations. Section 4 is devoted to the analysis of the global properties of the IGM and WHIM emission, while Section 5 focuses on our predictions for the oxygen line statistics. We summarize our results and draw our conclusions in Section 6. Unless stated otherwise, when referring to solar metal abundances and relative element yields we will assume the results reported in Asplund et al. (2009).

## 2 THE HYDRODYNAMICAL SIMULATIONS

In this section we review the simulation set of Tornatore et al. (2010). We refer the reader to their original work for further details. The set consists of 8 cosmological hydrodynamical simulations performed with the TreePM-smoothed particle hydrodynamics (SPH) code GADGET-2 (Springel 2005) in a version that includes the implementation of the chemical enrichment of Tornatore et al. (2007). A summary of the main characteristics of the different runs is shown in Table 1.

For all the runs the cosmology assumed is a flat standard  $\Lambda$ CDM model consistent with the *WMAP-5* results (Komatsu et al. 2009), namely with  $\Omega_\Lambda=0.76$ ,  $\Omega_m=0.24$  and  $\Omega_b=0.0413$  for the matter-energy density parameter of the cosmological constant, total matter (dark and baryonic) and baryonic matter alone, respectively. The other cosmological parameters are a primordial power spectrum of the cold dark matter density perturbations with slope  $n_s = 0.95$  and normalization corresponding to  $\sigma_8=0.8$  and a Hub-

**Table 1.** Characteristics of the 8 simulations object of our study. Column 1: run name. Column 2: comoving length of the box ( $h^{-1}$  Mpc). Column 3: number of particles. Column 4: number of available snapshots in the interval  $0 < z < 1.5$ . Column 5: stellar IMF assumed. Column 6: feedback scheme (see more details in the text).

Run name	$L_{\text{box}}$	$N_{\text{dm}}, N_{\text{gas}}$	Snapshots	IMF	Feedback model
W (reference)	37.5	$256^3$	25	Kroupa	Winds
W <sub>75,512</sub>	75.0	$512^3$	6	Kroupa	Winds
W <sub>37,400</sub>	37.5	$400^3$	16	Kroupa	Winds
Way	37.5	$256^3$	25	Arimoto-Yoshii	Winds
Ws	37.5	$256^3$	25	Salpeter	Winds
NW	37.5	$256^3$	25	Kroupa	No winds
CW	37.5	$256^3$	25	Kroupa	Coupled winds
BH	37.5	$256^3$	25	Kroupa	BH-feedback, no winds

ble constant  $H_0 = 100 h \text{ km s}^{-1} \text{ Mpc}^{-1}$ , with  $h = 0.73$ . The gravitational softening is set to  $\varepsilon = 7.5 h^{-1} \text{ kpc}$  in comoving units at  $z > 2$  while at lower redshifts it is set to  $\varepsilon = 2.5 h^{-1}$  physical kpc.

We take the W run (see Table 1) as a reference model for comparison. This simulation follows the evolution of a box of  $L = 37.5 h^{-1}$  comoving Mpc per side, with  $2 \times 256^3$  particles for dark matter and gas: this results in a mass resolution of  $m_{\text{dm}} = 1.9 \times 10^8 h^{-1} M_{\odot}$  and  $m_{\text{gas}} = 3.6 \times 10^7 h^{-1} M_{\odot}$ , respectively. The choice of these parameters is the result of a compromise between the need to sample the perturbations on large scales and to achieve the resolution necessary to describe the dense environments where star formation and feedback take place. This run produced 43 outputs logarithmically equispaced in redshift from  $z = 4$  to  $z = 0$ . Since we are interested mainly in the WHIM emission and we do not expect significant contributions from high redshift gas, for the purpose of our work we considered only the 25 snapshots in the interval  $0 < z < 1.5$ .

The effect of a spatially uniform, redshift dependent UV background due to quasar radiation as in Haardt & Madau (1996) is considered (with helium heating rates enhanced by a factor of 3, see the discussion in Tornatore et al. 2010). This process is important when considering the evolution of the amount of matter in the WHIM phase (see, e.g., Davé et al. 2001). Star formation is modeled following the multiphase model of Springel & Hernquist (2003): in this prescription the SPH particles exceeding the density of  $n_{\text{H}} = 0.1 \text{ cm}^{-3}$  are considered to host a hot phase and a cold one in pressure equilibrium, with the latter assumed to host the star-forming regions. Every two-phase SPH particle spawns up to three generation of collisionless star particles in a stochastic way, each of them having about one third of the mass of the original gas one.

During this process the SPH particles are enriched following the prescription of Tornatore et al. (2007) that considers the formation of SN-II, SN-Ia together with low and intermediate mass stars in the AGB phase. The corresponding stellar yields are taken from Woosley & Weaver (1995), Thielemann et al. (2003) and van den Hoek & Groenewegen (1997) for the SN-II, SN-Ia and AGB, respectively. This code allows to follow independently the evolution of H, He and of 6 metal species, namely C, O, Mg, Si, S and Fe for every SPH particle. The formation of all the other elements is also computed in every gas particle though only globally, storing their total mass in a single variable in order to save memory and computation time. The IMF adopted is the one proposed by Kroupa (2001), with a multi-slope function of the form  $\varphi(m) \propto m^{-y}$ , with the index  $y$  varying in the range 0.3–1.7 from low to high masses.

Radiative cooling due to free-free interaction of the electrons and ions is computed using a primordial mix of H and He. In addition to that, cooling from heavy elements is followed adopting the cooling rates of Sutherland & Dopita (1993): in this scheme the global metallicity of every SPH particle, and not the individual elements, is considered assuming solar yields. However, as we will explain in detail in Section 3.2, we stress that for what concerns the results presented in this paper our mock emission spectra are computed considering all the elements provided by the Tornatore et al. (2007) code separately. We point out also that this cooling scheme assumes implicitly that the IGM is in collisional ionization equilibrium: although this is not completely true, this can be considered as a safe approximation of the gas ionization state in the densest regions of the WHIM that dominate the emission.

Galactic outflows are modeled following Springel & Hernquist (2003). Winds are assumed to blow from the star-forming regions with a mass loading rate  $\dot{M}_w = \eta \dot{M}_*$ , where  $\dot{M}_*$  is the star-formation rate of each multi-phase particle and the efficiency  $\eta$  is a free parameter (set to 2). SPH star-forming particles are then stochastically selected to become wind particles, with a velocity of  $v_w = 500 \text{ km/s}$  and are decoupled from the others allowing them to travel freely for  $10 h^{-1} \text{ kpc}$ . This allows the wind particles not to get stuck inside the dense star-forming regions.

In order to test the impact of the different parameters and assumptions of our reference W model, we analyze also the results of other 7 runs of Tornatore et al. (2010). It is important to note that all the simulations were run assuming the same initial conditions so that they actually follow the evolution of the same volume and matter (with the exception of W<sub>75,512</sub> that follows a larger volume) thus allowing a direct comparison between each other. In the following subsections we will describe these runs focusing on their differences with respect to the reference model.

## 2.1 Simulation parameters

The W<sub>75,512</sub> and W<sub>37,400</sub> runs assume the same reference model but with different volume size and resolution of the particles. These simulations can be used to assess how the limited volume and finite mass resolution affect our results.

The W<sub>75,512</sub> run has a box size of  $L = 75 h^{-1}$  comoving Mpc. The number of particles is augmented to  $2 \times 512^3$  in order to maintain the same resolution. On the other side the W<sub>37,400</sub> run follows the same volume but with higher resolution. The number of particles is increased to  $2 \times 400^3$ , achieving a resolution of  $m_{\text{dm}} = 5.0 \times 10^7 h^{-1} M_{\odot}$  and  $m_{\text{gas}} = 9.4 \times 10^6 h^{-1} M_{\odot}$ . The

softening is also reduced to  $\varepsilon = 4.8 h^{-1}$  comoving kpc at  $z > 2$  and  $\varepsilon = 1.6 h^{-1}$  physical kpc at  $z < 2$ .

The number of snapshots available for these runs is reduced. In the interval  $0 < z < 1.5$  we have 6 snapshots for  $W_{75,512}$  and 16 for  $W_{37,400}$ . However, our scheme for the reconstruction of the observed light-cone (see Section 3.1) allows us to minimize the impact of these differences.

## 2.2 Initial mass functions

The Way and Ws runs differ from the reference model as the IMF adopted for these two runs are from Arimoto & Yoshii (1987) and Salpeter (1955), respectively. Changing the IMF implies a modification of the proportion of the SN types which reflects into different element ratios: top-heavier models produce a relatively higher number of SN-II and therefore are expected to provide more oxygen with respect to iron and carbon.

Indeed, the Way run shows a global value of  $[C/O]=-0.3$  for the WHIM at  $z = 0$  while the W and Ws runs have values close to  $-0.15$ . All the three models show a similar behavior of the redshift evolution with  $[C/O]$  ratios growing with time due to the increasing contribution of SN-Ia (see the corresponding discussion in Tornatore et al. 2010).

## 2.3 Feedback models

The NW, CW and BH runs adopt a modified feedback scheme with respect to our reference W run. In the NW run galactic winds are simply turned off, while the CW simulation keeps wind particles hydrodynamically coupled with the other ones (more details about the effect of coupled winds on star-forming systems can be found in Dalla Vecchia & Schaye 2008).

The BH run assumes no winds but includes the energy feedback associated to supermassive black-holes (SMBH) following Springel (2005) and Di Matteo et al. (2005). In brief, SMBHs are computed as sink particles hosted by haloes of mass higher than  $M_{\text{th}} = 10^{10} h^{-1} M_{\odot}$  that grow with a rate of

$$\dot{M}_{\text{BH}} = \min(\dot{M}_{\text{B}}, \dot{M}_{\text{Edd}}), \quad (1)$$

where  $\dot{M}_{\text{B}}$  and  $\dot{M}_{\text{Edd}}$  are the Bondi-Hoyle-Lyttleton accretion rate (see, e.g., Bondi 1952) and the Eddington rate, respectively. The energy rate injected into the surrounding gas is computed as  $\dot{E}_{\text{feed}} = \epsilon_{\text{r}} \epsilon_{\text{f}} \dot{M}_{\text{BH}}^2$ , being  $\epsilon_{\text{r}}$  and  $\epsilon_{\text{f}}$  the two free parameters representing the radiative efficiency and the fraction of energy coupled to the gas, respectively. These values are set to  $\epsilon_{\text{r}} = 0.1$  and  $\epsilon_{\text{f}} = 0.05$  with which Di Matteo et al. (2005) were able to reproduce the observed relation between BH mass and velocity dispersion of the bulge.

We refer the reader to the detailed discussion in Tornatore et al. (2010) about the effects of these models on the properties of the IGM. As a general remark, here we point out that NW and BH models show a stronger star formation rate (SFR) at higher redshift with respect to our reference run. Starting at  $z \sim 3$  the BH feedback causes a heavy suppression of star-formation, getting closer to the W simulations, while for the NW the SFR stays higher even at later epochs. It is important to highlight also that BH feedback is able to affect significantly the properties of collapsed objects causing the IGM to be more diffuse at all scales.

## 3 THE SIMULATED LIGHT-CONES

Extracting observables from the outputs of LSS simulations requires a non-trivial post-processing analysis: indeed, one needs to reconstruct all the volume of the past light-cone as seen by an observer located at  $z = 0$  in order to account for all the matter that contributes to the integrated signal up to a given redshift.

For the purpose of estimating the properties of the WHIM emission, we decide to consider the interval  $0 < z < 1.5$ : this is enough to account for most of the expected signal (see Roncarelli et al. 2006; Takei et al. 2011). Then we compute the X-ray emission spectra associated to the gas elements present in the light-cone volume, we integrate them along the line-of-sight and, finally, we produce mock 3D-maps in which every pixel contains the spectrum as seen by a telescope.

In this Section we describe in detail the different steps of this procedure.

### 3.1 Reconstructing the light-cone volume

The method described here is an improvement of the one adopted in Roncarelli et al. (2006) and Ursino et al. (2010) for the X-ray emission of the LSS (see also similar applications for estimates of the SunyaevZel'dovich effect in da Silva et al. 2000, 2001; White et al. 2002; Zhang et al. 2002; Roncarelli et al. 2007), since it includes a more general randomization scheme and a more precise procedure for the redshift sampling (as in Roncarelli et al. 2010).

We reconstruct the light-cone volume by replicating the outputs of the simulations along the line of sight up to the redshift limit of  $z = 1.5$ . With the cosmological parameters assumed here (see Section 2) this corresponds to a comoving distance of  $d_{c,\text{lim}} = 3206 h^{-1} \text{Mpc}$ , which is 86 times the length of our simulation boxes (43 for the  $W_{75,512}$  run). When considering large distances one needs also to take into account the evolution of structure formation by using the different simulation snapshots. To this purpose for a given distance from the observer we chose the output that better approximates the age of the Universe at that epoch. Since in our case we have more cubes to stack than available outputs, most of the cubes will correspond to the same snapshot than their neighbor(s). When a snapshot change intervenes the cube is split into two slices at the corresponding distance.

In order to avoid the repetition of the same structures in our maps, every cube undergoes a series of randomization procedures. First we give to every axis a 50 per cent probability of being reflected, then we chose randomly the axis order. Once this is done, we exploit the periodic boundary conditions of our simulations to select a position inside the cube which is then put in its center. Finally we introduce a rotation of a random angle along the line of sight only if the distance from the observer is small enough to ensure that the projected cube encloses all the map surface. As in our previous works, the slices corresponding to different snapshots but belonging to the same cube undergo the same randomization process to preserve power on large scales.

### 3.2 Computing the X-ray spectra and maps

For every SPH particle that falls inside the light-cone we compute its spectrum deriving it from its physical variables. We adopt the

APEC emission model (Smith et al. 2001, version 2.0<sup>1</sup>) which assumes that the emitting gas is an optically thin plasma in collisional ionization equilibrium. We create a series of emission tables by using the VAPEC implementation on XSPEC (version 12.6.0) that allows to separate the contribution of the different elements. More in detail, for every element considered in our simulations (H, He, C, O, Mg, Si, S, Fe and the sum of all the others<sup>2</sup>, as described in Section 2) we extract three-dimensional tables  $s_{\text{el}}(z, T, E)$  with fixed metallicity and normalization in which two variables are the redshift and temperature and the third one is the energy channel. Then the flux as a function of energy  $E$  is computed for the  $i$ -th SPH particle as

$$F_i(E) = \frac{n_{e,i} n_{\text{H},i} V_i}{4\pi d_{c,i}^2} \sum_{\text{el}} X_{\text{el},i} s_{\text{el}}(z_i, T_i, E), \quad (2)$$

where  $n_{e,i}$  and  $n_{\text{H},i}$  are the electron and hydrogen number density, respectively, for each particle,  $V_i$  is its physical volume and  $d_{c,i}$  is its comoving distance from the observer. The redshift  $z_i$  and the temperature  $T_i$  of the SPH particle are used to interpolate the value of  $s_{\text{el}}(z_i, T_i, E)$  from the tables. The abundance of each element is defined as

$$X_{\text{el},i} \equiv A_{\text{el}} \frac{n_{\text{el},i}}{n_{\text{H},i}}, \quad (3)$$

where  $A_{\text{el}}$  is the element atomic mass in units of the proton mass and  $n_{\text{el},i}$  is the number density of the element provided by the code<sup>3</sup>.

Finally, in order to obtain the surface brightness the flux of every particle computed from eq. (2) is distributed in the map pixels by integrating analytically the SPH smoothing kernel (the details of the procedure are explained in Ursino et al. 2010).

### 3.3 The light-cone set

The method described above allows us to compute a set of 3-d mock spectral maps (i.e. the surface brightness  $SB(\vec{\theta}, E)$ , as a function of the position in the sky  $\vec{\theta}$  and energy  $E$ ) from which we extract our results.

To assess the statistical robustness of our results we construct 20 different light-cones by varying the initial numerical seeds necessary for the randomization process (see Section 3.1). Each of them is applied to all of the simulation runs, ensuring that every light-cone represents the same comoving volume (except for the  $W_{75,512}$  run), simulated with different physical prescriptions. This is important because it allows us to compare directly the results of our simulations without dealing with uncertainties associated to cosmic variance. On the whole we obtain 640 outputs with different characteristics summarized in Table 2.

In our analysis we distinguish between the properties of the IGM as a whole and of the WHIM. Here we adopt the definition of WHIM as the gas with temperature in the range  $10^5$ – $10^7$  K and density contrast  $\delta < 1000$ . We advise the reader that not all the authors adopt the same definition: in some works the WHIM is defined only with respect to the temperature cut, in particular this applies to Roncarelli et al. (2006) and to Tornatore et al. (2010) with

which we will make an extensive comparison. In practice, the difference consists in the inclusion or not of the warm-hot dense gas that roughly corresponds to galaxy groups. As a reference, with our definition the WHIM accounts for 33 per cent of the total baryonic mass at  $z = 0$  in the W run.

Given the redshift limit of  $z < 1.5$ , the maximum angular extension of the maps is fixed by the box length and corresponds to about 40 (80 for the  $W_{75,512}$  run) arcmin, however we chose to compute maps of 30 arcmin per side in order to avoid problems caused by border effects: this size roughly corresponds to the double of the CDFs, so that every mock map covers four times as much sky surface.

The first two sets of mock maps, as indicated in Table 2, have 512 pixels per side which corresponds to a resolution of 3.52 arcsec. The spectra span the energy range 0.3–10 keV and are sampled with bins of 50 eV for energies lower than 2 keV. At higher energies we only compute the surface brightness of four 2 keV-wide bands. The results of these two sets will be compared mainly with *Chandra* and *XMM-Newton* data in the following section.

Our method of spectra computation, as described by eq. (2), allows us to separate the contribution of the different chemical elements. Taking advantage of this, we can artificially “switch off” the emission of all other elements in order to focus on the properties of oxygen only. To this purpose we compute two other sets of mock maps that include only the signal from this element. Since our goal is to study line emission, we increase the spectral resolution to 1 eV, while reducing the energy range to an upper limit of 1 keV and the angular resolution to  $\sim 1$  arcmin. We produce other two sets (for the IGM and the WHIM) with this method and use it to predict oxygen line counts (see Section 5).

## 4 PROPERTIES OF THE X-RAY EMISSION

We show in Fig. 1 the expected IGM surface brightness in the 0.3–0.8 keV band for a single light-cone with 4 different feedback schemes. As said in the previous section, with our volume reconstruction procedure we ensure that our maps reproduce exactly the same structures (i.e. the same objects in the same positions), with no difference associated to cosmic variance.

The emission is dominated by galaxy clusters, with peaks that have similar values for all the models ( $\sim 1 \text{ ph s}^{-1} \text{ cm}^{-2} \text{ deg}^{-2}$ ). A significant fraction of the maps has a fainter surface brightness from  $10^{-3}$  down to  $10^{-7} \text{ ph s}^{-1} \text{ cm}^{-2} \text{ deg}^{-2}$ . In the W model the haloes are significantly more diffuse: given the relatively small size of our simulation volume we should consider this as representative of the effect at the galaxy group scale. When turning winds off (NW model) clusters have sharper peaks, while the CW model produces an intermediate effect. In the BH model the cluster emission is significantly lower: the strong energy injection at early epochs increases considerably the entropy of the gas causing a suppression of gas accretion from high redshift. As a result smaller haloes are disrupted while for bigger ones only the central peaks are present (see the discussion in Tornatore et al. 2010). On the contrary, with this model low surface brightness regions are slightly brighter: apart from cluster centers all pixels stay roughly within 2-3 orders of magnitudes in surface brightness. Due to the very strong effect on galaxy clusters and groups, this model has to be considered as an extreme and non-realistic case. It is, however, useful as a case study to understand the effect of this kind of feedback.

The maps of Fig. 2 show the surface brightness of the same light-cones but considering the WHIM only: the difference with re-

<sup>1</sup> We are aware of the error in the calculation of some ions present in this version of the code. We checked that its impact on our results is negligible.

<sup>2</sup> The relative abundances of the elements not considered individually are computed from Asplund et al. (2009).

<sup>3</sup> In the formula of eq. (2) the abundance is generalized also for hydrogen for which, of course,  $X_{\text{H}} \equiv 1$ .

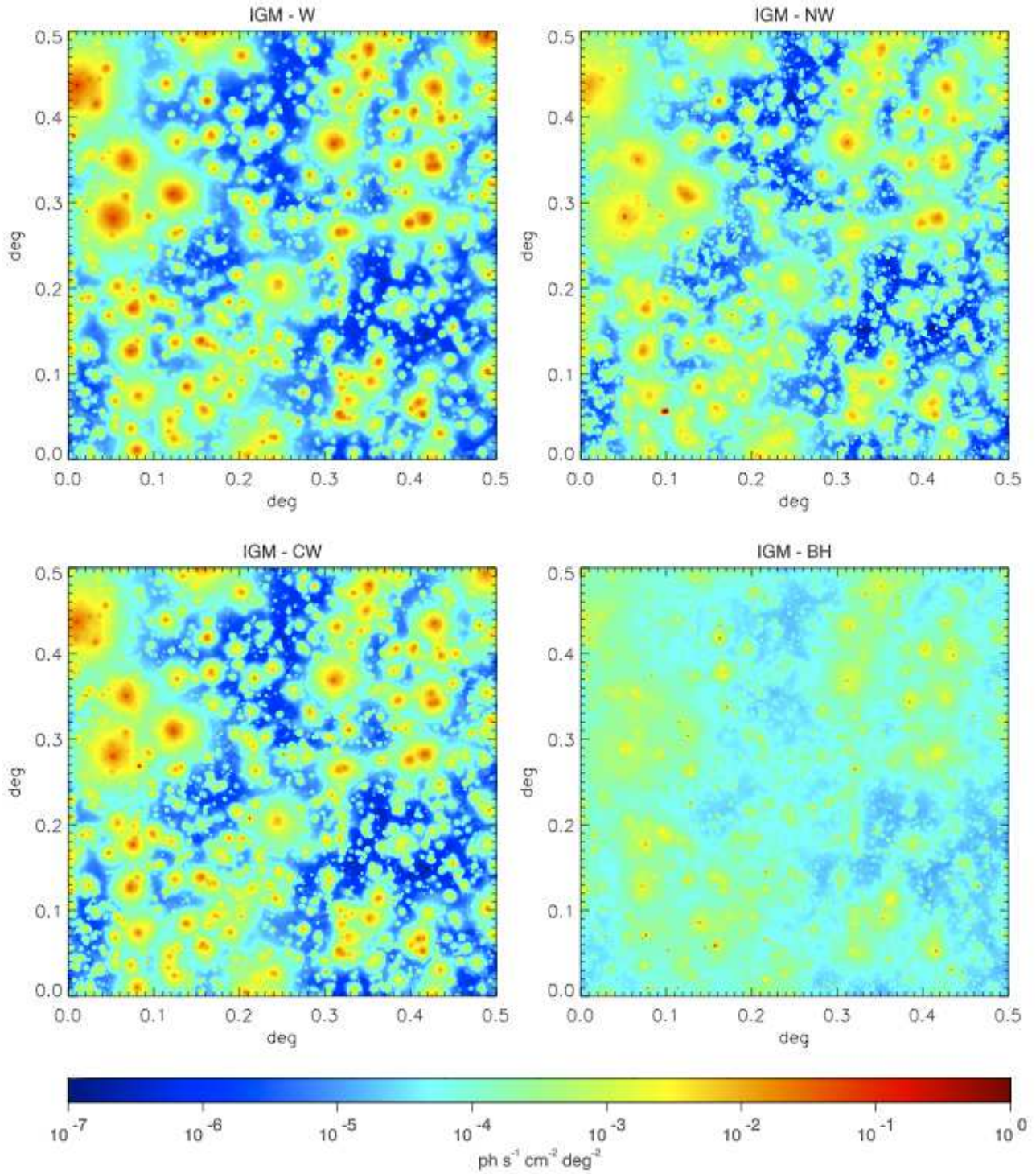


**Figure 1.** Surface brightness of the IGM (i.e. all the gas) in the 0.3–0.8 keV band. The maps are 0.5 deg per side and represent the same light cone simulated with different feedback schemes: galactic winds (W model, top left), no winds (NW model, top right), coupled winds (CW model, bottom left) and black-holes feedback (BH model, bottom right).

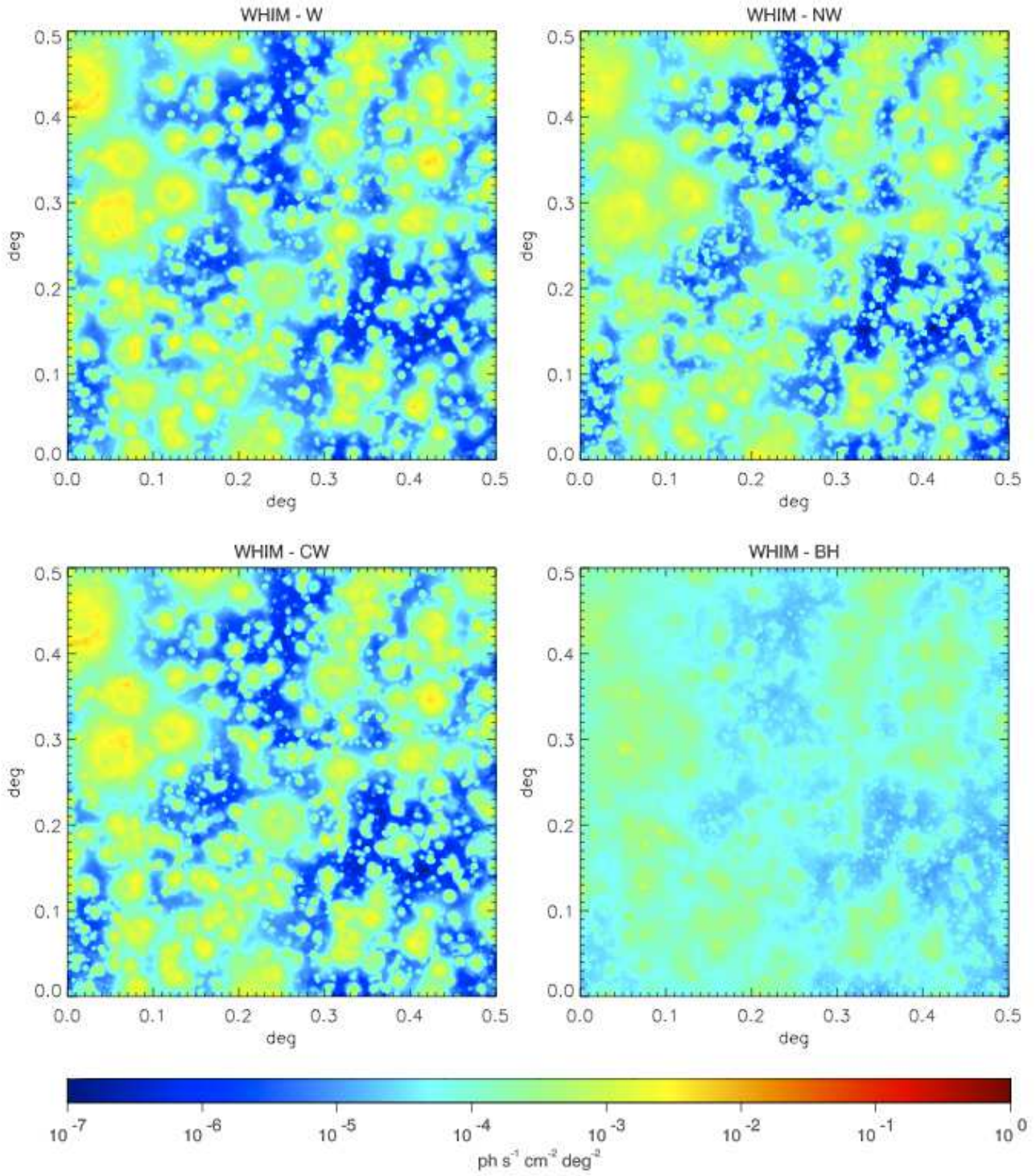


Figure 2. The same as Fig. 1 but for the WHIM (i.e. gas with  $10^5 \text{ K} < T < 10^7 \text{ K}$  and  $\delta < 1000$ ).

**Table 2.** Summary of the sets of 3-d spectral maps created for our studies. In all cases the redshift interval is  $0 < z < 1.5$ . Column 1: total number of mock maps (the number of simulation runs times the number of independent light-cones). Column 2: gas phase, IGM corresponds to all of the gas present in the simulation outputs, WHIM corresponds to the gas with temperature in the range  $10^5 - 10^7$  K and density contrast  $\delta < 1000$ . Column 3: chemical elements considered. Column 4: angular size of the maps. Column 5: angular resolution. Column 6: energy range of the spectrum. Column 7: energy resolution for the  $E < 1$  keV bins.

$N$ (sims $\times$ cones)	Gas phase	Elements	Map size (deg)	Ang. resolution (arcsec)	Energy range (keV)	En. res. ( $E < 1$ keV) (eV)
$8 \times 20$	IGM (all)	All	0.5	3.52	0.3–10	50
$8 \times 20$	WHIM	All	0.5	3.52	0.3–10	50
$8 \times 20$	IGM (all)	O	0.5	56.25	0.3–1	1
$8 \times 20$	WHIM	O	0.5	56.25	0.3–1	1

spect to the previous ones is of course the absence of the hot bright cluster centers. These images show that even if our definition of WHIM includes the density cut at  $\delta < 1000$ , cluster and group outskirts close to the virialized regions are still present. However, these structures can be considered below the detection limit of the CDFs (see Section 4.1 and Fig. 4). It is important to note that even when excluding artificially the hot gas directly from the simulations, no filamentary structure is clearly visible in these maps. This is due to the superimposition of the structures of the cosmic web along the line of sight with the effect of self-washing out. Also in these maps the most important differences are in the BH model, where the WHIM appears more diffuse and fainter than in the other cases. The effect of enhancing the surface brightness of the faintest pixels has little impact on the possibility of detecting these regions since they still fall well below the limits of current instruments. The images of the other models (not shown in these figures) do not differ significantly from our reference one (W model).

We analyse the effect of feedback on the spectral properties of the IGM and the WHIM with the plots shown in Fig. 3 and with the corresponding surface brightness in different bands shown in Table 3. When considering a large box ( $W_{75,512}$ , top panel), the global IGM emission is about 20 per cent higher at all energies due to the presence of more massive clusters. On the contrary, no significant change is produced when considering the WHIM emission, as an indication that our box size is large enough to sample the LSS perturbations that influence the WHIM physics. The opposite effect applies when increasing the resolution of our simulations ( $W_{37,400}$ ): almost no difference can be seen for the IGM signal while the WHIM emission increases by  $\sim 10$  per cent. This is mainly due to the effect of resolution on metal formation/emission, as we will discuss in Section 5. On the whole we can safely conclude that the limited box size and resolution of our simulations have a negligible impact on the expected surface brightness of the WHIM.

The main impact of assuming different IMFs (Way,  $W_s$ , central panel) is the fact that a top-heavy one, like the one from Arimoto & Yoshii (1987), produces much more SN-II, and to a lesser extent also more SN-Ia. This increases the abundance of all the metals and particularly O which is mainly ejected by SN-II (we address the reader to the discussion in Tornatore et al. 2007, for more details). This explains our results for the WHIM: since O has the peak of its emission lines at  $T \approx 10^6$  K and energies around 0.5 keV, the largest impact is seen in the 0.3–0.8 keV band surface brightness, where the WHIM is 20 per cent brighter in the Way run with respect to the  $W_s$  one (see also our results on line-emission in Sect. 5). On the other side, we observe an opposite trend in the

surface brightness of the IGM, with the top-light Salpeter (1955) IMF having the highest emission. This result is due to the fact that when considering a top-light IMF less metals are produced, thus decreasing the cooling efficiency, and providing a higher fraction of hot  $T > 10^7$  K gas that dominates the emission.

The most important variations are introduced when considering the different feedback schemes (bottom panel). Galactic winds have a twofold effect: on one side they suppress the peak emission in the central regions of clusters and, at the same time, they populate their outer parts with more material. Part of this gas is ejected at early epochs before the clusters form, while the remaining fraction is ejected directly in the intra-cluster medium significantly increasing the overall emission (see Fig. 1). As a result the IGM surface brightness is increased by a factor of  $\sim 2$  at all energies when comparing the NW and W runs, with the CW run constituting an intermediate scenario. The same applies to the WHIM emission but with only a  $\sim 20$  per cent increase from the NW to the W run. This is particularly evident at  $E < 0.8$  keV where oxygen emission dominates, indicating that winds are able to spread metals in the regions at intermediate temperatures.

On the other side, BH feedback greatly suppresses the emission, for both IGM and WHIM. In the IGM the difference range from a factor of 5 at lower energies up to one order of magnitude in the 2–10 keV band, while for the WHIM it is a factor of  $\sim 3$ . This is the result of the strong BH winds that prevent gas from collapsing and suppress star formation.

We also estimate the cosmic variance associated to our results by computing the standard deviation (quoted as error in Table 3) in 80 fields of  $225 \text{ arcmin}^2$ . For the IGM the cosmic variance is very high, comparable to the value itself: this happens because the presence of clusters and groups in the field dominates the total signal. Since the WHIM is dominated by the diffuse component its relative cosmic variance is lower, being of the order of 30 per cent in the 0.3–0.8 keV band, but still higher than the expected differences introduced by the various physical prescriptions.

We can compare our results for the IGM<sup>4</sup> also with our previous work (Roncarelli et al. 2006). Even if the feedback model of our W run is similar to the one adopted in that work (see Borgani et al. 2004), their total expected emission in the 0.5–2 and 2–10 keV bands is higher by a factor of 2 and 3, respectively. This difference is due to the larger volume of the simulation that allowed

<sup>4</sup> We do not compare our results on the WHIM given the different definitions (with and without the density cut at  $\delta < 1000$ ) adopted in the two works.



**Table 3.** Expected surface brightness (in units of  $10^{-12}$  erg s $^{-1}$  cm $^{-2}$  deg $^{-2}$ ) for the whole IGM (i.e. all the gas) and for the WHIM (i.e. gas with  $T = 10^5 - 10^7$  K and  $\delta < 1000$ ) in different X-ray bands. In each line the results are shown for the 8 different simulations as the mean computed over 20 independent light-cones (a total of 5 deg $^2$ ). The errors represent the standard deviations in fields equal to a quarter of the original maps (e.g. 225 arcmin $^2$ , close to the size of the CDFs).

Model	Surface brightness ( $10^{-12}$ erg s $^{-1}$ cm $^{-2}$ deg $^{-2}$ )							
	IGM (0.3–0.8) keV	WHIM	IGM (0.65–1) keV	WHIM	IGM (0.5–2) keV	WHIM	IGM (2–10) keV	WHIM
W	1.05±1.08	0.29±0.10	0.73±1.14	0.12±0.09	2.12±3.84	0.28±0.16	0.52±1.84	<0.01
W <sub>75,512</sub>	1.20±0.90	0.30±0.13	0.84±0.86	0.13±0.10	2.45±2.72	0.30±0.18	0.61±1.28	<0.01
W <sub>37,400</sub>	1.07±1.18	0.33±0.11	0.76±1.30	0.14±0.09	2.18±4.29	0.32±0.17	0.52±1.94	<0.01
Way	0.94±0.90	0.31±0.11	0.64±0.94	0.13±0.10	1.88±3.22	0.30±0.17	0.48±1.57	<0.01
Ws	1.17±1.08	0.26±0.09	0.82±1.14	0.10±0.07	2.32±3.34	0.24±0.13	0.46±1.03	<0.01
NW	0.57±0.50	0.24±0.08	0.38±0.53	0.11±0.08	1.06±1.84	0.24±0.13	0.26±0.94	<0.01
CW	0.84±0.71	0.28±0.10	0.55±0.73	0.12±0.09	1.59±2.53	0.28±0.16	0.39±1.27	<0.01
BH	0.22±0.12	0.10±0.03	0.11±0.13	0.04±0.03	0.31±0.40	0.09±0.05	0.06±0.16	<0.01

to better sample the high-mass tail of the mass distribution, thus obtaining brighter haloes that dominate the emission.

When comparing our WHIM results with the ones of Ursino et al. (2010) in the 0.65–1 keV band, our predictions are close to their  $0.15 \times 10^{-12}$  erg s $^{-1}$  cm $^{-2}$  deg $^{-2}$  obtained with a semianalytical characterization of the metallicity and a factor of  $\sim 2$  lower than their higher metallicity models. Even if these results can be considered to be in a broad agreement, their differences reflect the current uncertainties in how metals spread in the lower density regions and on the ability of hydrodynamical models to provide precise predictions on the WHIM emission. More precisely, the typical metal abundances associated to our WHIM phase are of the order of  $Z \approx 0.05 Z_{\odot}$ , that corresponds to a regime where the expected signal is roughly equally distributed between free-free and line-emission. When assuming a higher metallicity ( $Z = 0.1 - 0.15 Z_{\odot}$ ) the emission becomes metal-dominated and increases significantly, thus justifying the differences in the results with the higher metallicity models of Ursino et al. (2010).

#### 4.1 Comparison with the unresolved X-ray background

Our results can be compared with the upper limits provided by the unresolved X-ray background (UXRB) from Hickox & Markevitch (2007), who measured the diffuse emission in the CDFs after subtracting all possible contaminating sources. However, we must consider that a direct comparison between our IGM maps/spectra and the measured UXRB is not possible since our mock maps include also clusters and groups that have been identified and eliminated in the CDFs observations. On the other side, using our WHIM maps can lead to misleading results since our WHIM definition is based on the intrinsic thermodynamical properties of the SPH particles, that do not correspond to an observational criterium of source identification (see also the discussion in Roncarelli et al. 2006).

For these reasons we decide to adopt an observationally oriented approach to estimate the UXRB that corresponds to our simulations. Starting from our IGM maps/spectra (e.g., Fig. 1) we compute the photon counts in the 0.5–2 keV band expected from a *Chandra* Deep Field South (CDF-S) observation, by considering the ACIS-I response function at different energies (sampled in bins of 50 eV each). In order to simulate reliable *Chandra* images we added an isotropic level of background that takes into account the contribution of both galactic and particle background. We ne-

glected the contribution of undetected AGN/galaxies since, at flux limits of the CDF-S, their flux is completely described by point-like emission associated with optical or IR-detected galaxies, which were excluded by Hickox & Markevitch (2007). The images were then corrected for an average exposure of 4 Ms with an artificially added Poisson noise. The source identification has been performed by running a simple sliding cell detection with a cell size of 12 pixels and fixing a signal-to-noise ratio threshold of 4. We have then excluded all the regions within which the overall encircled signal from sources is above  $4\sigma$  with respect to the background. An example of the implementation of this method is shown in Fig. 4.

Once we have identified all the pixels corresponding to detected haloes, we compute the expected spectrum of the remaining regions for all the different light-cones and simulations. We show in Fig. 5 our results (averaged over the 20 light cones) for the W model for both the IGM and the WHIM and compare them with the observational estimates of Hickox & Markevitch (2007). The same comparison is shown in Table 4 for the emission in three different X-ray bands and for the other physical prescriptions.

When looking at the results for our reference model, the surface brightness per unit energy of the UXRb associated to the IGM is well represented by a power-law ( $SB \propto E^{-\gamma}$ ) with spectral index  $\gamma = 0.9$  (1.5, for the WHIM) in the 0.3–0.8 keV band, with a clear steepening at higher energies, up to  $\gamma = 2.5$  (3.8) in the 0.8–2 keV band. These values do not change significantly when other models are considered.

Through all the energy range our IGM predictions fall below the upper limits of the UXRb. At energies  $E \lesssim 0.7$  keV the expected emission of the whole IGM is more than an order of magnitude below the observed UXRb. This indicates that at soft energies other sources are the main contributors, likely the emission associated to local components (Galaxy and Solar System). For these reasons the search for LSS emission in the UXRb at these energies requires a subtraction of these foreground components with more than 10 per cent accuracy. A possible observational technique consists in relying on their different angular correlation of the two components, as we will discuss in Section 4.2.

On the contrary, we predict that at energies  $E \gtrsim 1$  keV a significant fraction (from 50 per cent to all) of the UXRb is due to the emission of the IGM. The high value of the cosmic variance (reported as error in Table 4) together with the low angular surface of the CDFs does not allow us to provide more precise estimates.

**Table 4.** The same as Table 3, but after subtracting clusters and groups identified in a mock CDF-S observation. The last line indicates the observational measurements of Hickox & Markevitch (2007) with relative errorbars.

Model	Surface brightness ( $10^{-12}$ erg s $^{-1}$ cm $^{-2}$ deg $^{-2}$ )					
	(0.5–2) keV		(0.65–1) keV		(1–2) keV	
	IGM	WHIM	IGM	WHIM	IGM	WHIM
W	0.57±1.31	0.17±0.21	0.23±0.54	0.08±0.12	0.23±0.67	0.04±0.06
Way	0.45±0.77	0.19±0.24	0.18±0.34	0.09±0.13	0.17±0.37	0.04±0.06
Ws	0.48±1.05	0.14±0.18	0.20±0.49	0.06±0.09	0.18±0.46	0.04±0.06
NW	0.33±0.42	0.16±0.17	0.14±0.19	0.08±0.10	0.11±0.20	0.03±0.04
CW	0.41±0.69	0.17±0.22	0.17±0.31	0.08±0.13	0.14±0.32	0.04±0.06
BH	0.20±0.18	0.08±0.05	0.08±0.07	0.04±0.03	0.07±0.09	0.02±0.01
Obs.	4.3±0.7		1.0±0.2		0.34±0.14	

When comparing our models with the different feedback and IMFs assumptions, the same considerations apply with respect to the discussion on Table 3: galactic winds increase consistently the expected IGM signal.

It is important to point out that in all cases the surface brightness associated to a diffuse WHIM component is less than half of the total IGM one, ranging from  $\sim 20$  per cent to  $\sim 40$  per cent from high to low energies, with the only exception of the 50 per cent of the Way model in the 0.65–1 keV band. This suggests that a consistent part of this signal is not associated with truly diffuse ( $\delta < 1000$ ) gas. In particular this becomes important at  $E \gtrsim 1$  keV where the majority of the UXRb due to the LSS is clearly associated to cluster outskirts and faint galaxy groups. However we must consider that LSS filaments also contain dense clumps that are excluded by our WHIM definition so, as a bottom line, we can consider our two estimates, IGM and WHIM, as bracketing the emission associated to the missing baryons component.

## 4.2 The angular correlation function

Given the relatively low surface brightness of the WHIM, one of the possible techniques to disentangle its signal from the other brighter components (e.g. Galactic emission) consists in performing a correlation function analysis. To this purpose we compute the angular (auto)correlation function ( $AcF$ )  $w(\theta)$  of the surface brightness in the 0.3–0.8 keV band.

We proceed as follows. First, for a given map we compute its surface brightness contrast

$$\delta(\vec{x}) \equiv (S_b(\vec{x})/\overline{S_b}) - 1, \quad (4)$$

where  $S_b(\vec{x})$  is the surface brightness at the position  $\vec{x}$  and  $\overline{S_b}$  is the average of the map. Then we compute the angular correlation function as

$$w(\theta) = \langle \delta(\vec{x})\delta(\vec{x} + \vec{\theta}) \rangle. \quad (5)$$

With this definition a value of  $w(\theta) = 0$  corresponds to a random uncorrelated field.

We show in Fig. 6 our results for the IGM and the WHIM and for our 4 different feedback schemes. As expected (see, e.g., Roncarelli et al. 2006; Ursino et al. 2011), the IGM correlates significantly up to angular scales of 2–3 arcmin, which correspond to the typical size of galaxy clusters and groups. At larger scales it drops rapidly to values consistent with zero ( $\theta \gtrsim 5$  arcmin). Again, the cosmic variance produces significant deviations (grey-shaded

area) from map to map. Galactic winds enhance the correlation signal of the IGM due to the higher relative clusters emission. The BH model produces a high correlation only at very low angular scales ( $\theta \lesssim 0.2$  arcmin), consistently with what appears from Fig. 1. On the other side, at  $\theta \gtrsim 2$ –3 arcmin the  $AcF$  is shallower due to the presence of a diffuse emission associated to gas ejected from galactic haloes at early epochs. When neglecting galactic winds (NW) high correlations at  $\theta \gtrsim 2$ –3 arcmin are found as well. This is associated to the presence of small bright clumps that enhance the halo-halo correlation, and that show fainter peaks when winds are included (see the maps of Fig. 1). The WHIM  $AcF$  is lower by almost one order of magnitude at low angular scales but has a shallower slope making it comparable to the IGM one for  $\theta \sim 2$  arcmin. In this case, the different wind implementations (W, NW, CW) produce small variations in the  $AcF$ , of the order of 10 per cent.

We can compare our results with Galeazzi et al. (2009) who detected a putative WHIM emission by analysing the  $AcF$  of 6 different *XMM-Newton* fields in the 0.4–0.6 keV band<sup>5</sup>. In this comparison one must take into account the different normalization adopted with respect to our work: in fact, since they do not know *a priori* how much emission is associated to a diffuse component, they normalize  $w(\theta)$  to the total UXRb flux, including also the foreground contribution. We can obtain an order-of-magnitude estimate of the impact of this difference by using our results on the average 0.4–0.6 keV surface brightness associated to unresolved IGM emission (see Section 4.1) and compare it to their total UXRb from Hickox & Markevitch (2007): the ratio between the latter and the former is  $\sim 26$ , which translates into a difference in the normalization of the order of  $\sim 700$ . If we apply this correction to the data of Galeazzi et al. (2009), we obtain a value of  $w(\theta) \simeq 7$  for  $\theta=1$ –2 arcmin, that falls within a factor of  $\sim 3$  from our IGM results. Given the high values of relative errors and cosmic variance associated to these measurements, we can not obtain a more precise estimate, but we can conclude that our results appear in broad agreement with those by Galeazzi et al. (2009) at small angular scales. On the other side, we obtain a steeper slope of the  $AcF$  at large angular scales, suggesting the possible presence of a contribution from other components in their data.

<sup>5</sup> We checked that the changes in the  $AcF$  associated to the two different bands are negligible.

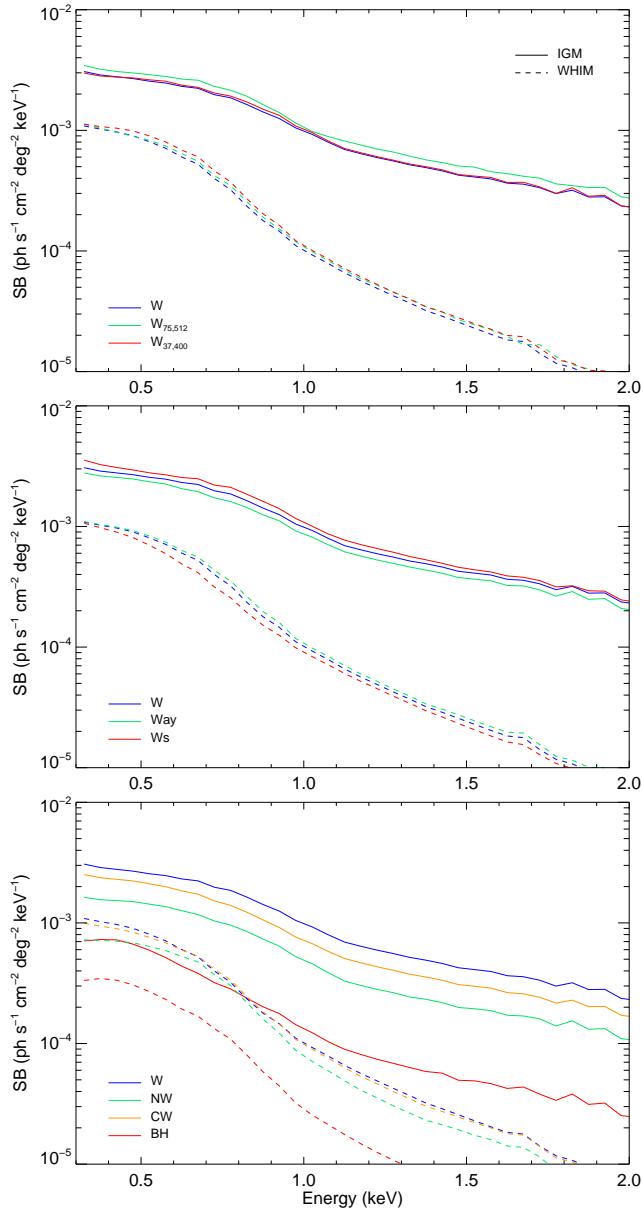


**Figure 3.** Expected spectra of the IGM (solid lines) and WHIM (dashed lines), computed as average over the 20 independent light-cones. In all plots the blue lines correspond to our reference model (W). Top panel: comparison with  $W_{75,512}$  (green) and  $W_{37,400}$  (red). Central panel: comparison with  $W_{\text{Way}}$  (green) and  $W_{\text{S}}$  (red). Bottom panel: comparison with  $NW$  (green),  $CW$  (orange) and  $BH$  (red).

## 5 OXYGEN LINE EMISSION

In this Section we focus on the properties of oxygen emission. In particular, we study the expected surface brightness due to OVII and OVIII that represent the ions with the most significant contribution at X-ray energies.

To this purpose we take advantage of our method for computing the spectra associated to the SPH particles described by eq. (2) that allows us to separate the emission from the different elements. As discussed in Section 3.3, we use the last two light-cones set listed in Table 2, which were computed with an energy resolution of 1 eV necessary for the analysis of single line emission. The en-

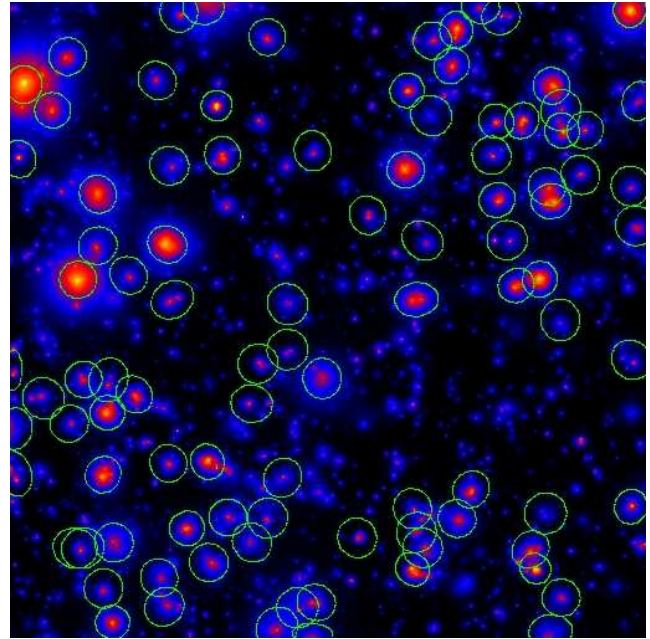


**Figure 4.** Sketch of the haloes (marked by the elliptical regions) identified in one of our mock maps. The map represents the surface brightness (on a logarithmic scale) at 0.3 keV and corresponds to the same light cone shown in the maps of Figs. 1 and 2.

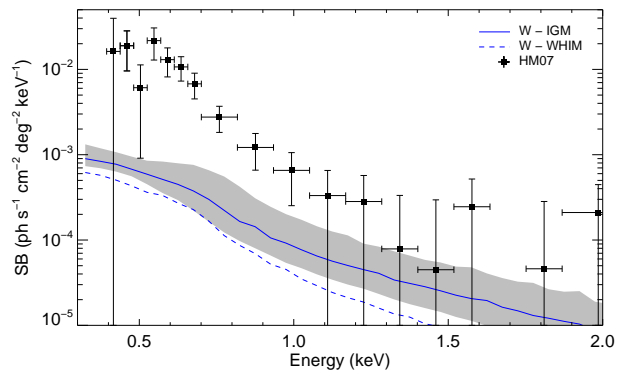


**Figure 5.** Expected spectrum of the diffuse XRB associated to extragalactic gas emission for the W model. The solid line corresponds to the whole (IGM) gas emission, the dashed line to the WHIM contribution. The lines correspond to the median relative to 80 different values computed on an area of  $225 \text{ arcmin}^2$  (e.g. CDFs), while the shaded region encloses the first and third quartile for the IGM. The black squares represent the data from Hickox & Markevitch (2007) with corresponding errorbars.

ergy range considered here (0.3–1 keV) allows us to enclose all of the most important OVII and OVIII lines up to  $z \simeq 0.9$ , with no significant contribution from OVI. In order to save memory, these O emission spectra have been computed with a poorer angular resolution of  $\sim 1 \text{ arcmin}$ , but this does not introduce any systematics since the expected correlation of the IGM and WHIM signal does not rise significantly at lower angular scales (see Section 4.2). Moreover the expected angular resolution of the next-generation spectrographs (e.g., the *IXO/ATHENA* proposal<sup>6</sup>) is higher than this limit. An ex-

<sup>6</sup> <http://sci.esa.int/science-e/www/object/index.cfm?fobjectid=48729>

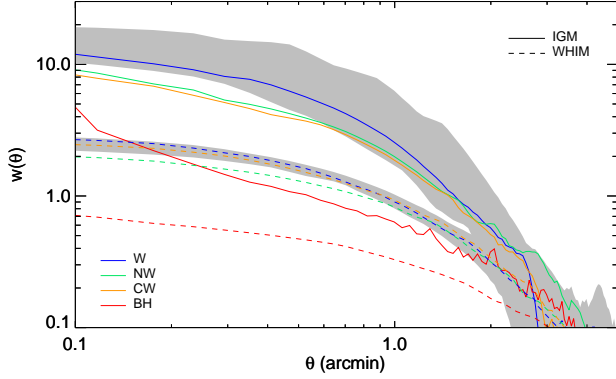


**Figure 6.** Angular correlation function of the IGM (solid lines) and the WHIM (dashed) for different feedback models: the reference W model (blue line), the NW model (green), the CW model (orange) and the BH one (red). Each curve represents the median computed over the 20 independent light-cones (area of  $900 \text{ arcmin}^2$ ) while the shaded regions enclose the first and third quartile.

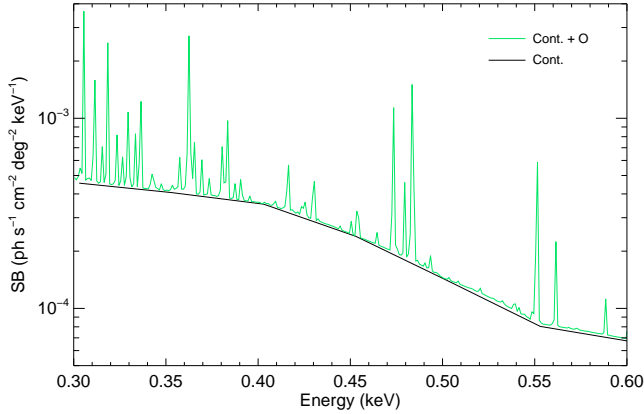


**Figure 7.** Example of a spectrum extracted from a pixel of  $1 \text{ arcmin}^2$  size, for the WHIM component only. The black line shows the continuum emission (i.e. including all the elements except oxygen) computed with 50 eV energy resolution. The green line represents the spectrum with the addition of oxygen emission, computed with 1 eV energy resolution to allow the identification of the lines.

ample of a WHIM spectrum computed with our method for both oxygen-line and continuum emission is shown in Fig. 7.

We compute the statistics of the expected number of O lines (OVII and OVIII added together) above a given surface brightness along the line of sight. We proceed in the following way. For a given pixel of our maps, that corresponds to a line-of-sight of  $0.88 \text{ arcmin}^2$  and extending in the range  $0 < z < 1.5$ , we consider its spectrum in the energy interval 0.3–1 keV and identify the 1 eV bins corresponding to a surface brightness higher than a threshold fixed to  $\text{SB}_{\text{th}} = 2 \times 10^{-6} \text{ ph s}^{-1} \text{cm}^{-2} \text{deg}^{-2}$  (safely below the detection limits of future instruments). Then, since an emission line can extend to more than 1 eV, we assign to a single line all the contiguous bins that fall above this threshold and sum their values to obtain the total surface brightness of the line itself. We repeat the same procedure for all the pixels and all the 20 different light-cones for both the IGM and the WHIM. We checked that the final results do not change significantly when degrading our angular resolution to  $\sim 2 \text{ arcmin}$  or when changing the value of  $\text{SB}_{\text{th}}$ .

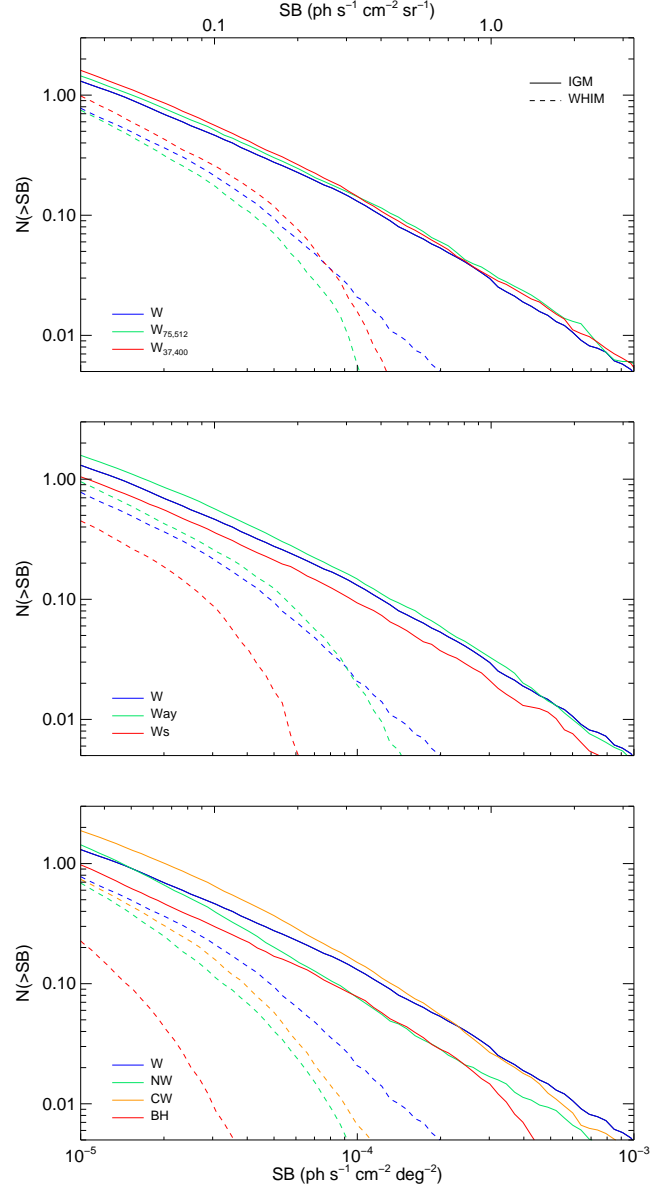


**Figure 8.** Expected counts of oxygen (OVII and OVIII) line emission associated to the IGM (solid lines) and WHIM (dashed lines) as a function of lines brightness. In all plots the blue lines correspond to our reference model (W). Top panel: comparison with  $W_{75,512}$  (green) and  $W_{37,400}$  (red). Central panel: comparison with Way (green) and  $W_s$  (red). Bottom panel: comparison with NW (green), CW (orange) and BH (red).

Fig. 8 shows the expected number counts of oxygen lines for our reference run compared with the other ones. When considering the different simulation parameters (top panel) we see that increasing the mass resolution of the simulation by a factor of  $\sim 4$  enhances the expected line counts for the IGM by  $\sim 20$  per cent. This is due to improved capability of resolving the high density regions that host the star-forming metal-rich gas and are therefore bright line-emitters. The effect is also present when considering the WHIM oxygen lines in the faint ( $\text{SB} < 10^{-4} \text{ ph s}^{-1} \text{cm}^{-2} \text{deg}^{-2}$ ) end. This suggests that a high resolution is mandatory in this kind of analysis and is more desirable than a large simulation volume.

The different IMFs (central panel) produce changes in the amount of SN-II and, consequently, on the total amount of oxy-

gen released by stars. With the top-heavy Arimoto & Yoshii (1987) IMF (Way model) the increased amount of SN-II produces significantly more oxygen. If we take as a reference a surface brightness detection threshold of  $3 \times 10^{-5} \text{ ph s}^{-1} \text{ cm}^{-2} \text{ deg}^{-2}$  (a possible goal of next-generation instruments), this translates into  $\sim 20$  per cent more detected lines for both IGM and WHIM. The opposite effect happens when adopting the Salpeter (1955) IMF (Ws).

The changes introduced by different feedback schemes (bottom panel) are also relevant. When suppressing galactic winds (NW) metals remain more concentrated in the cold star-forming regions where they are not able to emit significantly: this results in a factor of 2 less expected lines for the IGM. The CW model shows trend for the IGM similar to the W model, with a small increase for fainter lines. When looking at the WHIM curves, the effect of metal transport due to galactic winds can be seen with the higher amount of lines expected with respect to the NW model, that reaches an order of magnitude for brighter ( $\text{SB} > 10^{-4} \text{ ph s}^{-1} \text{ cm}^{-2} \text{ deg}^{-2}$ ) lines. Coupled winds are not able to diffuse efficiently metals in the low density regions, resulting in a number of lines closer to the NW run than to the W one. Considering the BH feedback, the expected line counts are significantly smaller for both IGM and WHIM. Again, this is the result of the early energy feedback that suppresses the gas collapse resulting in the IGM having less dense structures. This effect is even more remarkable in the WHIM.

## 5.1 Comparison with other models

Apart from the differences introduced by the various feedback mechanisms, we can compare the results of our reference run with the expected oxygen line counts estimated by Takei et al. (2011) and Cen & Fang (2006). On the whole, the number of oxygen lines that we estimate is significantly lower with respect to their results. If we consider the B1 model of Takei et al. (2011) and a reference surface brightness of  $0.1 \text{ ph s}^{-1} \text{ cm}^{-2} \text{ sr}^{-1}$ , they obtain a value of  $N \simeq 2$  for the sum of OVII and OVIII lines in the IGM case and  $N \simeq 1$  for the WHIM<sup>7</sup>, while our reference model predicts 0.5 and 0.25 respectively, a factor 3–4 lower. As a consequence, with our results the amount of WHIM emission lines detectable by future X-ray instruments is significantly reduced. If we consider a resolution element of 2.6 arcmin, our W model predicts  $\sim 100$  detections per square degree of either OVII or OVIII lines from the WHIM. The reason of this discrepancy has to be searched in the different recipe adopted to describe the metal enrichment of the gas. Takei et al. (2011) adopt a post-processing method assigning a metallicity to the SPH particles as a function of overdensity: in particular, they use the results of Cen & Ostriker (1999) who estimated a relation of the form  $Z \propto \delta^{1/2}$ . If we compare it to what was shown in Tornatore et al. (2010) we can see that this results in a factor of  $\sim 2$  less metals at overdensities  $\delta < 10^4$ . In addition to that, if we take into account also the differences in the relative element abundance, our model presents a O/Fe mass ratio of  $\sim 2.5$  while Takei et al. (2011) adopt solar yields from Anders & Grevesse (1989) which correspond to a mass ratio of 5.2. This adds another difference by a factor of 2 in the abundance of oxygen. At a first approximation, given the linear dependence of line emissivity on the element abundance, this translates into a factor of  $\sim 4$  in line surface brightness

<sup>7</sup> The authors show the value of  $\Delta N/\Delta z$ . Since their redshift interval is  $0 < z < 0.5$  here we consider that the contribution from lines associated to higher redshift emitters is negligible.

that is sufficient to explain the differences with their work. In order to verify this hypothesis we run a test light-cone implementing their  $Z - \delta$  relation and, as expected, we obtained results similar to Takei et al. (2011).

We can also compare our results with Cen & Fang (2006) who computed the expected oxygen lines by using a hydrodynamical simulation. Even if they provide only the value of  $dN/dz$  at  $z = 0$ , we can estimate that our numbers are smaller, coherently to what said about Takei et al. (2011). Again, part of the difference is due to the different element yields: Cen & Fang (2006) artificially augment the oxygen abundance of their model (see the discussion in their Section 2) to reach a value of O/Fe close to 2 times solar<sup>8</sup>. Such a high value is ruled out by current estimates from observed galaxy clusters (Tamura et al. 2004; Simionescu et al. 2009). In addition to that, their simulation is able to spread more efficiently the metals outside the hot and dense regions, resulting in more oxygen in the thermodynamical conditions that correspond to bright OVII and OVIII emission. This issue is connected to the current uncertainties in the hydrodynamical codes and particularly in the feedback implementation. More in detail, it has been shown that introducing a coupled winds scheme on simulations at galactic scales can impact galactic properties as well as the amount of ejected material (Dalla Vecchia & Schaye 2008). Moreover also the implementation of momentum-driven winds in hydrodynamical simulations can modify the star-formation history and increase the amount of metals ejected at earlier epochs (see, e.g., Oppenheimer & Davé 2006; Tesfari et al. 2009). However, given the complex interplay between wind efficiency and star formation regulation, it is difficult to determine whether these models might reduce the discrepancy between our results and the ones of Cen & Fang (2006). In this framework, an interesting comparison can be provided by estimates from OVI absorption systems that are, however, beyond the scope of this paper.

## 6 CONCLUSIONS

In this paper we have analyzed a set of cosmological hydrodynamical simulations presented in Tornatore et al. (2010) that include a detailed treatment of chemical enrichment of the IGM. The aim is to provide a description of the expected X-ray emission of the WHIM, with focus on the influence of different feedback mechanisms, namely initial mass functions, galactic winds and black hole feedback.

Our results can be summarized as follows.

- (i) Galactic winds have a strong impact on the expected signal of the WHIM and the IGM in general: with our assumptions ( $v_w = 500 \text{ km/s}$ ,  $\eta = 2$ ) the surface brightness is enhanced by a factor of 2 through all the energy range of interest (0.3–10 keV). This is due to the ability of winds to push gas and metals in cluster outskirts and outside, making lower density regions brighter.
- (ii) On the other side BHs, acting at earlier epochs, can prevent the IGM to collapse in dense structures suppressing significantly the expected emission of clusters and WHIM.
- (iii) All of our models predict that the expected contribution from non-resolved LSS structures (galaxy groups, WHIM) is below the upper limits of the UXRb (Hickox & Markevitch 2007). At energies  $E \lesssim 0.7 \text{ keV}$  they account for only  $\sim 10$  per cent of the

<sup>8</sup> We converted their ratio of 1.67 referred to Anders & Grevesse (1989) yields to the ones of Asplund et al. (2009).

UXRB, indicating that Galactic components dominate, while at  $E \gtrsim 1$  keV, they account from half to all of the signal, with significant field-to-field differences expected due to cosmic variance.

(iv) The WHIM shows an angular correlation function  $w(\theta) > 1$  up to scales of 2-3 arcmin, with very low variations due to feedback effects or cosmic variance. At low angular scales ( $\theta = 1 - 2$  arcmin), our results are in broad agreement with the observations of Galeazzi et al. (2009), while for larger angles we obtain lower values.

(v) The expected oxygen (OVII and OVIII) line counts depend significantly on the choice of the feedback models. In particular, the number of detectable line counts is increased by a factor of 3 by GWs and by 20 per cent when assuming a top-heavy IMF (Arimoto & Yoshii 1987). We obtain also a significant enhancement by increasing the mass resolution of the simulation.

(vi) With our simulations we predict a number of detectable oxygen emission lines lower by a factor of 3-4 with respect to the predictions of other works (Cen & Fang 2006; Takei et al. 2011) due to differences in the implementation of chemical enrichment in the hydrodynamical codes. This has to be subject of further investigations and has to be considered a part of current uncertainties in the modelisation of the WHIM properties. However, if our results were confirmed, observing O lines from the WHIM might be a difficult task even for the upcoming X-ray observatories.

As a conclusion, our work confirms the importance of the use of hydrodynamical simulations in the modelisation of the LSS properties, together with the comparison with observations. In particular, we highlighted how the new generation of X-ray telescopes could provide constraints on both the missing baryon component and the mechanisms of star-formation and feedback that affect the WHIM. In this framework, it will be interesting to extend the results of our work also to the absorption properties in the X-ray and UV frequency range.

## ACKNOWLEDGMENTS

Most of the computations necessary for this work have been performed thanks to the Italian SuperComputing Resource Allocation (ISCRA) of the *Consorzio Interuniversitario del Nord Est per il Calcolo Automatico* (CINECA). We acknowledge financial contributions from contracts ASI-INAF I/023/05/0, ASI-INAF I/088/06/0, ASI I/016/07/0 COFIS, ASI Euclid-DUNE I/064/08/0, ASIUni Bologna-Astronomy Dept. Euclid-NIS I/039/10/0, PRIN MIUR “Dark energy and cosmology with large galaxy survey”, the European Commissions FP7 Marie Curie Initial Training Network CosmoComp (PITN-GA-2009-238356), by the PRIN-MIUR09 “Tracing the growth of structures in the Universe” and by the PD51 INFN grant. We thank an anonymous referee that provided useful comments which contributed to improve the presentation of our results. We acknowledge useful discussions with A. Baldi, S. Di Meo, S. Ettori, D. Fabjan, R. Hickox, L. Lovisari, R. Smith, L. Tornatore and E. Ursino. We are grateful to R. Hickox for providing us the data on the UXR. The parallelization of the light-cone simulator code has been done with the assistance of C. Gheller. A special thank goes to D. Fabjan for the help in dealing with simulation outputs.

## REFERENCES

Anders E., Grevesse N., 1989, *GeCoA*, 53, 197

- Arimoto N., Yoshii Y., 1987, *A&A*, 173, 23  
 Asplund M., Grevesse N., Sauval A. J., Scott P., 2009, *ARA&A*, 47, 481  
 Bertone S., Schaye J., Dalla Vecchia C., Booth C. M., Theuns T., Wiersma R. P. C., 2010, *MNRAS*, 407, 544  
 Bond J. R., Kofman L., Pogosyan D., 1996, *Nat*, 380, 603  
 Bondi H., 1952, *MNRAS*, 112, 195  
 Borgani S., Murante G., Springel V., Diaferio A., Dolag K., Moscardini L., Tormen G., Tornatore L., Tozzi P., 2004, *MNRAS*, 348, 1078  
 Bregman J. N., 2007, *ARA&A*, 45, 221  
 Buote D. A., Zappacosta L., Fang T., Humphrey P. J., Gastaldello F., Tagliaferri G., 2009, *ApJ*, 695, 1351  
 Cen R., Fang T., 2006, *ApJ*, 650, 573  
 Cen R., Ostriker J. P., 1999, *ApJ*, 514, 1  
 Cen R., Ostriker J. P., 2006, *ApJ*, 650, 560  
 da Silva A. C., Barbosa D., Liddle A. R., Thomas P. A., 2000, *MNRAS*, 317, 37  
 da Silva A. C., Barbosa D., Liddle A. R., Thomas P. A., 2001, *MNRAS*, 326, 155  
 Dalla Vecchia C., Schaye J., 2008, *MNRAS*, 387, 1431  
 Danforth C. W., Shull J. M., 2005, *ApJ*, 624, 555  
 Danforth C. W., Shull J. M., 2008, *ApJ*, 679, 194  
 Davé R., et al., 2001, *ApJ*, 552, 473  
 Di Matteo T., Springel V., Hernquist L., 2005, *Nat*, 433, 604  
 Fang T., Buote D. A., Humphrey P. J., Canizares C. R., Zappacosta L., Maiolino R., Tagliaferri G., Gastaldello F., 2010, *ApJ*, 714, 1715  
 Fang T., Marshall H. L., Lee J. C., Davis D. S., Canizares C. R., 2002, *ApJ*, 572, L127  
 Fujimoto R., Takei Y., Tamura T., Mitsuda K., Yamasaki N. Y., Shibata R., Ohashi T., Ota N., Audley M. D., Kelley R. L., Kilbourne C. A., 2004, *PASJ*, 56, L29  
 Galeazzi M., Gupta A., Ursino E., 2009, *ApJ*, 695, 1127  
 Haardt F., Madau P., 1996, *ApJ*, 461, 20  
 Hickox R. C., Markevitch M., 2007, *ApJ*, 661, L117  
 Kaastra J. S., Werner N., Herder J. W. A. d., Paerels F. B. S., de Plaa J., Rasmussen A. P., de Vries C. P., 2006, *ApJ*, 652, 189  
 Kirkman D., Tytler D., Suzuki N., O’Meara J. M., Lubin D., 2003, *ApJS*, 149, 1  
 Komatsu E., Dunkley J., Nolte M. R., Bennett C. L., Gold B., Hinshaw G., Jarosik N., Larson D., Limon M., Page L., Spergel D. N., Halpern M., Hill R. S., Kogut A., Meyer S. S., Tucker G. S., Weiland J. L., Wollack E., Wright E. L., 2009, *ApJS*, 180, 330  
 Komatsu E., et al., 2011, *ApJS*, 192, 18  
 Kroupa P., 2001, *MNRAS*, 322, 231  
 Mathur S., Weinberg D. H., Chen X., 2003, *ApJ*, 582, 82  
 Nicastro F., Mathur S., Elvis M., Drake J., Fang T., Fruscione A., Krongold Y., Marshall H., Williams R., Zezas A., 2005a, *Nat*, 433, 495  
 Nicastro F., Mathur S., Elvis M., Drake J., Fiore F., Fang T., Fruscione A., Krongold Y., Marshall H., Williams R., 2005b, *ApJ*, 629, 700  
 Oppenheimer B. D., Davé R., 2006, *MNRAS*, 373, 1265  
 Penton S. V., Stocke J. T., Shull J. M., 2004, *ApJS*, 152, 29  
 Rasmussen A. P., Kahn S. M., Paerels F., Herder J. W. d., Kaastra J., de Vries C., 2007, *ApJ*, 656, 129  
 Rauch M., 1998, *ARA&A*, 36, 267  
 Roncarelli M., Moscardini L., Borgani S., Dolag K., 2007, *MNRAS*, 378, 1259

- Roncarelli M., Moscardini L., Branchini E., Dolag K., Grossi M., Iannuzzi F., Matarrese S., 2010, *MNRAS*, 402, 923
- Roncarelli M., Moscardini L., Tozzi P., Borgani S., Cheng L. M., Diaferio A., Dolag K., Murante G., 2006, *MNRAS*, 368, 74
- Salpeter E. E., 1955, *ApJ*, 121, 161
- Simionescu A., Werner N., Böhringer H., Kaastra J. S., Finoguenov A., Brügggen M., Nulsen P. E. J., 2009, *A&A*, 493, 409
- Smith R. K., Brickhouse N. S., Liedahl D. A., Raymond J. C., 2001, *ApJ*, 556, L91
- Springel V., 2005, *MNRAS*, 364, 1105
- Springel V., Hernquist L., 2003, *MNRAS*, 339, 289
- Sutherland R. S., Dopita M. A., 1993, *ApJS*, 88, 253
- Takei Y., Henry J. P., Finoguenov A., Mitsuda K., Tamura T., Fujimoto R., Briel U. G., 2007, *ApJ*, 655, 831
- Takei Y., Ursino E., Branchini E., Ohashi T., Kawahara H., Mitsuda K., Piro L., Corsi A., Amati L., den Herder J. W., Galeazzi M., Kaastra J., Moscardini L., Nicastro F., Paerels F., Roncarelli M., Viel M., 2011, *ApJ*, 734, 91
- Tamura T., Kaastra J. S., den Herder J. W. A., Bleeker J. A. M., Peterson J. R., 2004, *A&A*, 420, 135
- Tescari E., Viel M., Tornatore L., Borgani S., 2009, *MNRAS*, 397, 411
- Thielemann F.-K., Argast D., Brachwitz F., Hix W. R., Höflich P., Liebendörfer M., Martinez-Pinedo G., Mezzacappa A., Panov I., Rauscher T., 2003, *Nuclear Physics A*, 718, 139
- Tornatore L., Borgani S., Dolag K., Matteucci F., 2007, *MNRAS*, 382, 1050
- Tornatore L., Borgani S., Viel M., Springel V., 2010, *MNRAS*, 402, 1911
- Tripp T. M., Sembach K. R., Bowen D. V., Savage B. D., Jenkins E. B., Lehner N., Richter P., 2008, *ApJS*, 177, 39
- Ursino E., Branchini E., Galeazzi M., Marulli F., Moscardini L., Piro L., Roncarelli M., Takei Y., 2011, *MNRAS*, 414, 2970
- Ursino E., Galeazzi M., Roncarelli M., 2010, *ApJ*, 721, 46
- van den Hoek L. B., Groenewegen M. A. T., 1997, *A&A Supp.*, 123, 305
- Weinberg D. H., Miralda-Escude J., Hernquist L., Katz N., 1997, *ApJ*, 490, 564
- Werner N., Finoguenov A., Kaastra J. S., Simionescu A., Dietrich J. P., Vink J., Böhringer H., 2008, *A&A*, 482, L29
- White M., Hernquist L., Springel V., 2002, *ApJ*, 579, 16
- Woosley S. E., Weaver T. A., 1995, *ApJS*, 101, 181
- Yao Y., Shull J. M., Danforth C. W., 2011, *ApJ*, 728, L16
- Zappacosta L., Maiolino R., Mannucci F., Gilli R., Schuecker P., 2005, *MNRAS*, 357, 929
- Zappacosta L., Mannucci F., Maiolino R., Gilli R., Ferrara A., Finoguenov A., Nagar N. M., Axon D. J., 2002, *A&A*, 394, 7
- Zappacosta L., Nicastro F., Maiolino R., Tagliaferri G., Buote D. A., Fang T., Humphrey P. J., Gastaldello F., 2010, *ApJ*, 717, 74
- Zhang P., Pen U.-L., Wang B., 2002, *ApJ*, 577, 555